Project no. NMP4-CT-2004-013684

FORCETOOL

Multipurpose Force Tool for Quantitative Nanoscale Analysis and Manipulation of Biomolecular, Polymeric and Heterogeneous Materials

Instrument:: **STREP**
Thematic priority: **NMP-3**

Publishable Final Activity Report

Period covered: **from 1 February 2005 to 31 January 2008**
Date of preparation : **5 March 2008**

Start date: **1 February 2005** Duration: **3 years**

Project coordinator name: **Ricardo García**
Project Organisation name: **Consejo Superior de Investigaciones Científicas (CSIC)**

Table of Contents

Consortium

The consortium brings together ***leading research*** groups in advanced dynamic force methods, synthesis of nanostructured materials, nanopatterning and manipulation methods, simulation and modelling of nano and meso-scale systems with *the world leader company* (an SME) in cantilever fabrication and a established SME in electronics and software design. The wide range of skills and competences needed to design and prototype the bi-modal AFM as well as to develop the multimaterial methodology explains the size of the FORCETOOL consortium (9 participants). The ***academic/research members*** of the consortium have a consolidated experience in transforming ***basic research results*** into ***technological implications***.

Two SMEs are involved in FORCETOOL. Nanoworld is the world leader on cantilever fabrication. It has a key role in FT: design and fabrication of tailored cantilevers for bi-modal excitation. Eldisa is a established company in electronics and software design. Its role is to design and fabricate the bi-modal control unit.

Prof. Ricardo García, Consejo Superior de Investigaciones Científicas (CSIC) (co-ordinator),
Dr. Fabio Biscarini, Consiglio Nazionale delle Ricerche (CNR)
Prof. Julius Vancso, University of Twente (UT),
Dr. Robert Stark, Ludwig-Maximilians-Universität (LMU) MU,
Prof. Robert Magerle, Chemnitz University of Technology (CUT),
Dr. Rubén Pérez, Universidad Autónoma de Madrid (UAM),
Dr. Thomas Sulzbach, NanoWorld,
Prof. Peter Hinterdorfer, University of Linz (JKU),
Ignacio Rodríguez, Electrónica y Diseño (Eldisa)

Contact
Ricardo García
forctool@imm.cnm.csic.es
www.imm.cnm.csic.es/ForceTool

Project execution

Summary main objectives

FORCETOOL (FT) proposes to develop a ***multipurpose tool*** for ***quantitative*** nanoscale analysis and ***manipulation*** of biomolecular, polymeric and heterogeneous surfaces. Key features of the proposed instrument are ***1 nm*** spatial resolution and ***1 pN*** force sensitivity; operation in ***technological*** relevant ***environments*** (air or liquids) and with ***no impact*** on the sample surface. The multifunctionality and flexibility of FT will enable characterization, control or manipulation of structures on a nanometer-scale, so it will open new approaches for manufacturing at molecular and nanoscale levels. This tool is based on two innovative concepts: (i) the bi-modal AFM and (ii) the multimaterial methodolody. The ***bi-modal AFM concept*** considers the cantilever as a three dimensional object with several resonance modes, in particular two. The concept ***departs radically*** from the ***established*** principles of ***dynamic force microscopy*** (only the fundamental mode is considered). The double excitation allows to separate topography from composition contributions in the experimental data. Furthermore, the ***bi-modal AFM*** is about ***two orders*** of ***magnitude*** more ***sensitive*** to force variations than state of the art ***tapping mode*** AFMs.

The ***multimaterial methodology*** will allow to transform the amplitude, frequency or phase shift changes measured by the instrument into quantitative information about the sample properties. The multimaterial methodology has both a ***general framework*** to describe dynamic force microscopy interactions and ***specific codes*** to be used with different materials such as inorganic materials, biomolecules, polymers or molecular architectures.

Specifically the key goals are:

Topography, composition analysis and manipulation of biomolecules, polymers and heterogeneous surfaces; operation in air or liquids so it will be compatible with industrial environments; 1 nm spatial resolution and 1 pN force sensitivity; compatible with existing atomic force microscopes, so an additional module could up-grade their capabilities.

Major Impacts: (1) FORCETOOL will develop a new multipurpose tool for quantitative nanoscale analysis and manipulation of heterogeneous surfaces in relevant technological environments (2). It will improve European competitiveness by establishing the technological and scientific foundations of the next generation of advanced scanning probe microscopes.

Executive summary of results

Bimodal AFM. We have designed, manufactured and tested several bi-modal AFM excitation/detection prototypes. The bimodal AFM have successfully imaged proteins (antibodies) in air and liquid environments. We have also characterized the performance of the instrument under different excitation forces (mechanical and electrostatic), cantilever types, and different samples, such as biomolecules, polymers and layered materials. The force sensitivity of the instrument has been determined about 0.2 pN, i.e., a factor 10 better than conventional tapping mode AFM. In addition, we have demonstrated that the bimodal AFM concept is compatible with existing AFMs and with nanotomography methods. A multilevel theoretical approach have been applied to understand bimodal AFM operation. This approach has involved continuous modeling, finite element simulations and analytical approaches. The analytical model identifies the virial and the energy dissipated by the tip-surface forces as the parameters responsible for the material contrast. The agreement obtained among the theory, experiments and numerical simulations validates the model.

We have also demonstrated that dynamic AFM operation at higher harmonics renders high resolution images of biological membranes and virus capsids in liquids. We have also shown that higher harmonics imaging is also compatible with molecular recognition process.

Multimaterial Methodology. We have developed a method to identify the mechanism of energy dissipation at the nanoscale. The method requires the determination of the energy dissipated on the sample surface as a function of the oscillation amplitude while the tip approaches the surface. The representation of the dissipated energy and, in particular, its derivative with respect to the amplitude, dynamic-dissipation curves hereafter, characterizes the dissipation process. Three different nonconservative processes were studied: surface energy hysteresis, viscoelasticity and long-range dissipative interfacial interactions. The method is being applied to characterize the organization of thin polymer films.

Multiscale theoretical simulations have also provided insight into the relationship between forces, molecular re-orientations and energy dissipation processes. We have performed a combined experimental and multiscale theoretical approach to establish the atomistic origins and hence the contrast, of the dissipative processes occurring in phase-imaging. First-principle simulations show that the configuration space sampled by the tip depends on whether the tip approaches or withdraws from the surface. The quantitative agreement obtained between simulations and experiments demonstrates that the above asymmetry is the origin of the observed contrast. The asymmetry arises because the presence of energy barriers among different bonding configurations.

Bimodal Atomic Force Microscopy

The development of the Bimodal AFM microscope and its applications has involved the participation of several ForceTool partners, especifically, Eldisa, LMU, JKU, CNR, CUT, NWs and CSIC).

Bimodal AFM excitation/detection unit (CSIC, Eldisa)

Bimodal AFM imaging is based on the simultaneous excitation of two flexural modes of the microcantilever. The root mean square *rms* amplitude of the first mode is fed back to the controller for topography imaging while the phase shift of first and second mode are recorded and plotted to detect compositional variations. The amplitude of the first mode will be used to map the topography while either the phase shift or the amplitude of the second mode will be used to increase the force sensitivity to map material properties. Initially, FT is focussed on the first two eigenmodes of the microcantilever, although, it is possible to excite any other pair of modes.

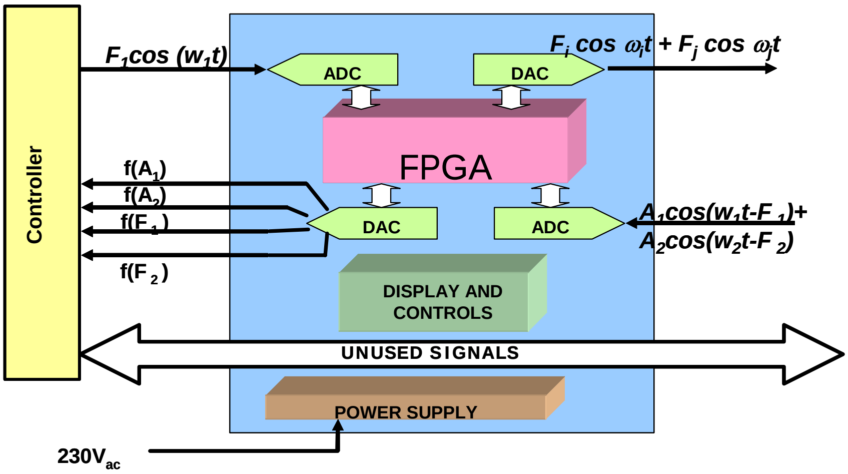

Figure 1. Schematics of the bimodal AFM excitation(/detection unit.

Figure 1 shows a block diagram of the experimental set-up to perform the simultaneous excitation and the phase shift representation of the first two normal modes. The key element is the simultaneous excitation of the microcantilever to its first and second resonances by a mechanical force described by,

$$F_{exc}(t)=F_1 \cos \omega_1 t+ F_2 \cos \omega_2 t \qquad (1)$$

where ω_1 and ω_2 are the angular frequencies of the first and second flexural modes of the free cantilever. The output signal of the first mode is used to image the topography of the sample while the phase shift of the second mode is used to map changes in the composition of the atoms or molecules under the tip. Figure 2 shows the photodiode signal and its Fourier transform under bimodal AFM operation.

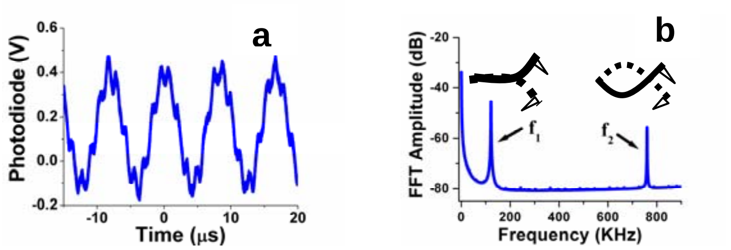

Figure 2. (a) Photodiode signal Ander bi-modal operation. (b). Fast fourier transform of the signal shown in (a).

An image of the first bimodal AFM controller is shown in Fig. 3. To operate an AFM under bi-modal excitation requires to interface the AFM controller and AFM head with the bimodal unit (Fig. 4). The bimodal AFM excitation/detection unit includes detection and excitation modules.

Figure 3. Left circuit board of the prototype and prototype of the bi-modal AFM unit

The CSIC and ELDISA partners have teamed up to manufacture six bimodal AFM excitation/detection units (Fig. 5). Those units have been delivered to several FORCETOOL partners: CNR, CUT, LMU and NWs.

Figure 4. Bimodal AFM microscope. The instrument combines a comercial AFM platform with the bimodal AFM controller developed in the ForceTool Project.

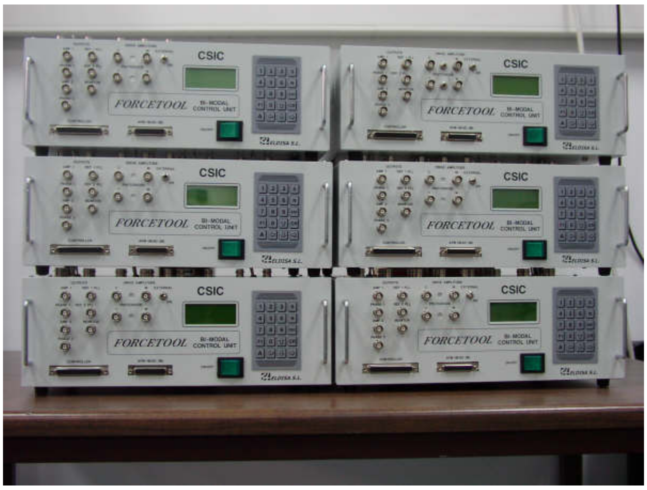

Figure 5. Picture of six of the bimodal AFM units manufactured by the CSIC and Eldisa within the ForceTool Project.

Bimodal AFM operation (CSIC, LMU, NWs)

The proper operation of the bimodal AFM microscope has involved a variety of activities such as the design of tailored cantilevers for bimodal AFM operation (see Fig. 6 for some of the bimodal cantilever geometries), the simulation of the nonlinear noise of the instrument, the optimum ratio between amplitudes or the dependence of the experimental parameters amplitude and phase shifts with the tip-surface distance.

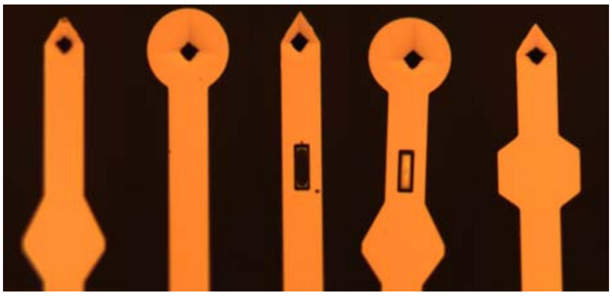

Figure 6. Geometries of some of the cantilever tailored for bimodal AFM operation. Design and manufacture by NWs.

To optimize the performance of bi-modal AFM operation, we have studied the influence on the bi-modal AFM contrast on the first and second mode amplitude ratio. Figure 7 shows a sequence of regular (left) tapping-mode AFM and bi-modal AFM (right) images of a sample made of sexithiophene islands deposited on silicon. The images show the changes of the bimodal contrast between silicon and T6 for different amplitudes of the second mode. A more exhaustive quantitative analysis is shown in Fig. 8. The data shows that for a fixed amplitude of the first mode, the contrast given by the second mode increases by decreasing the amplitude of the second mode (but always above of the noise level).

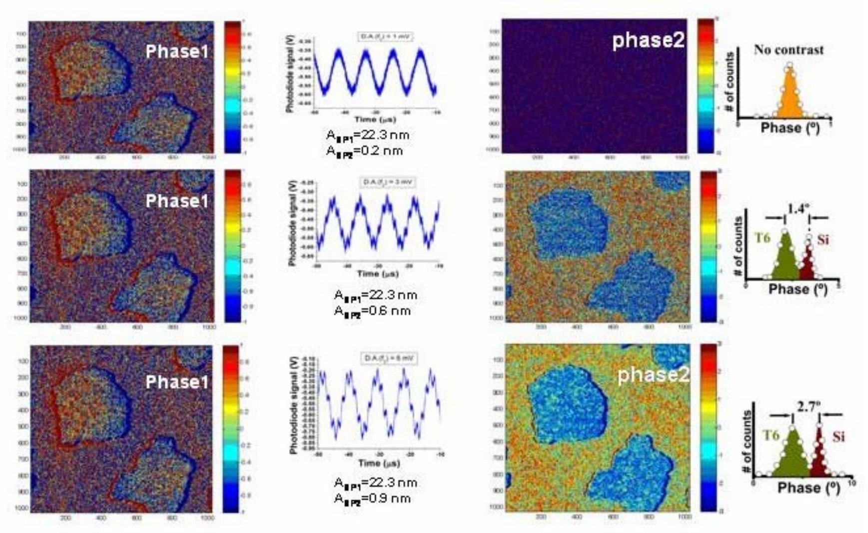

Figure 7. Dependence of the bi-modal phase shift contrasto n the amplitude ratio of first and second modes. Bimodal AFM experiments on T6 islands deposited on silicon.

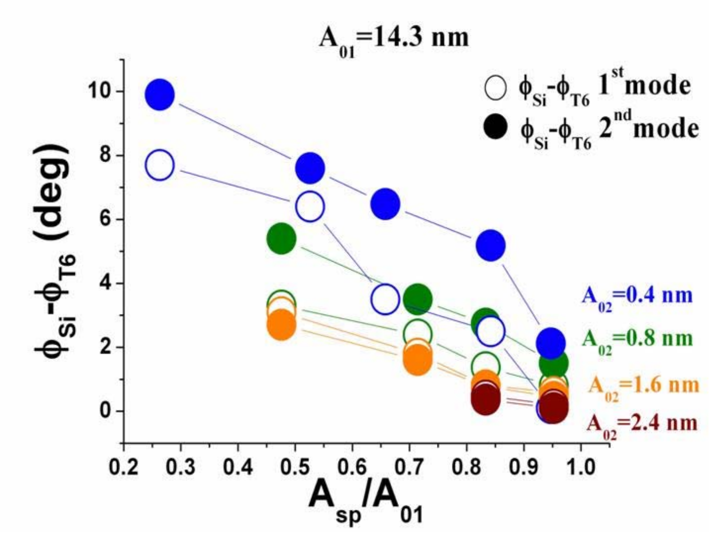

Figure 8. Dependence of the phase shift contrast between T6 and silicon (1st and 2nd modes) as a function of the amplitude of the second mode.

We also studied the dependence of amplitude and phase versus distance curves are shown in Figure 9. The red curves in Fig. 9 correspond to the curves recorded under bimodal excitation. An amplitude ratio of 10 was used. The deflection signals of all four experiments are essentially the same. The amplitude decrease of the first eigenmode does not seem to be influenced by the addition oscillation at the second eigenmode. However, the phase shift of the oscillation at the first eigenmode shows crosstalk from the higher frequency modulation, but it is also qualitatively unchanged. In the right column, the second eigenmode signals, we observe drastic changes. The amplitude is damped from the point of first contact of the first eigenmode distance curve. This is reasonable, since the tip of the cantilever encounters contact with the surface once during each oscillation. Thus, the second eigenmode oscillation cannot be observed independently. In the phase shift signals, the influence on the second eigenmode becomes even more obvious.

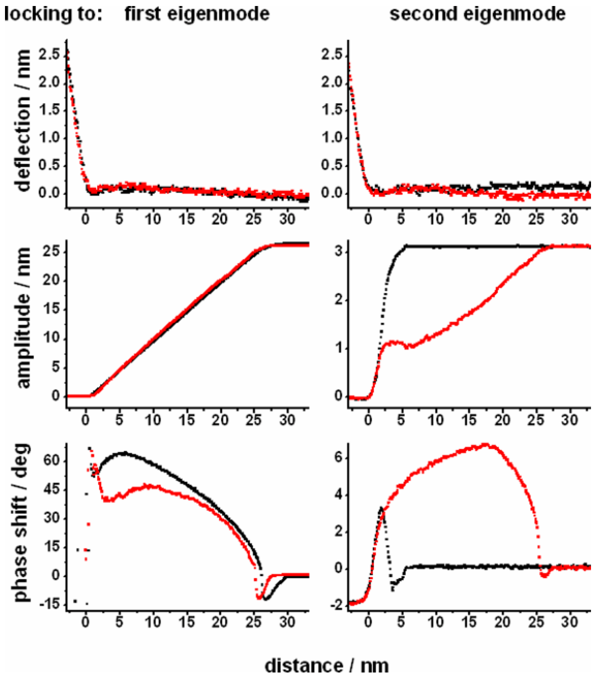

Figure 9. Distance curves using bimodal AFM on Si (100). Deflection, amplitude of oscillation, and phase shift are shown. Columns correspond to the reference signal of the lock-in amplifier, i.e. which eigenmode is analyzed (1st column – first eigenmode; 2nd column – second eigenmode). For the black curves, the first and second eigenmodes have been driven exclusively. These curves have been used for calibration purposes. The red curves show the dependencies when both first and second eigenmode are driven simultaneously.

Comparison between bimodal and tapping mode AFM methods (CSIC)

To asses and compare the performance of the bimodal AFM we have taken images of conjugated molecular materials with the bimodal AFM and a conventional amplitude modulation AFM. Figure 10 shows the topography and phase shift images of several T6 monolayers deposited on a silicon surface. Topography and phase images are taken simultaneously. The size and shape of the T6 islands on silicon makes them ideal samples to test the compositional sensitivity of an AFM. Figures 10b and 10c show the phase images of the T6 islands on silicon by recording respectively the phase shift variation of the first and second modes. The cross-section along the dashed line in Fig. 10b shows a $\Delta\phi_1=0.1^o$ contrast between the silicon and T6 (Fig. 10e), i.e., barely above the noise level (~0.05º). On the other hand, the phase shift difference obtained in the second mode is $\Delta\phi_2=0.9^o$ (Fig. 10e). The comparison between ϕ_1 and ϕ_2 cross-sections shows that the material contrast is enhanced by a factor 10 by

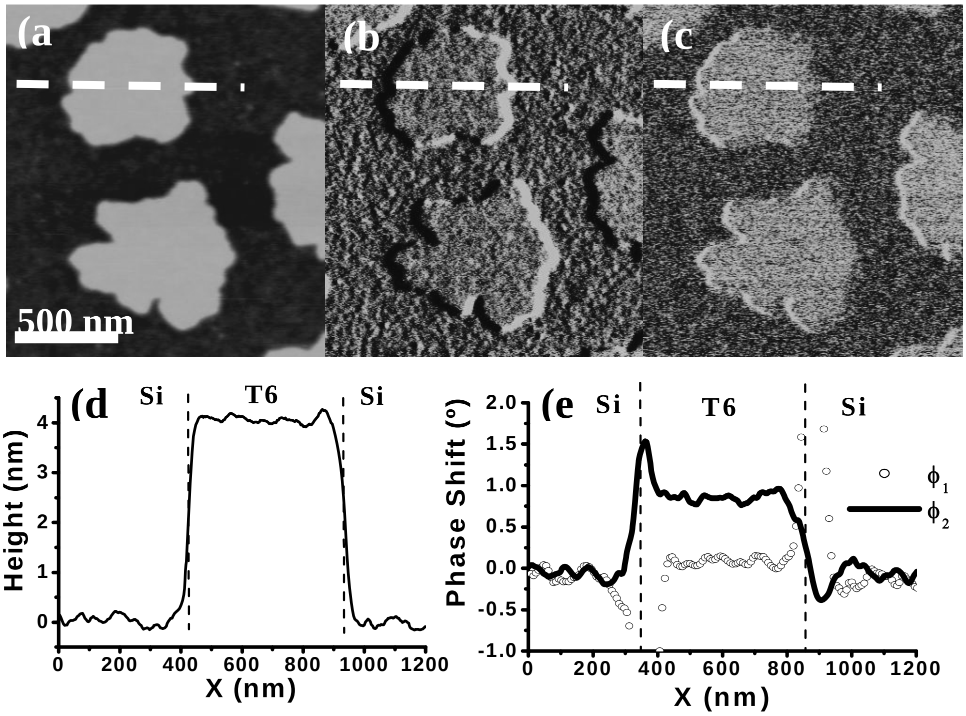

Figure 10 Topography and phase images of several T6 islands on silicon. (a) Topography, (b) first mode phase shift and (c) second mode phase shift. (d) Height variation across the dashed lines shown in (a). (e) Phase shift variations across the dashed line shown in (b) and (c). The vertical discontinuous lines show the edges of the T6 island. The contrast observed between silicon and T6 with the phase shift of the first mode is barely above the noise level. T6 and silicon are clearly distinguished by plotting the phase shift of the second mode. $A_1=14$ nm and $A_2=1.1$ nm; $f_1=106.7$ kHz and $f_2=667.4$ kHz; $A_{sp}=0.9\ A_{rms}$.

plotting the second mode phase shift. The peaks that appear in the phase shift cross-sections are topographic artifacts due to the finite time response of the feedback electronics. We remark that first and second mode phase images have been obtained under exactly the same conditions and forces.

Bi-modal AFM imaging applications (CSIC, LMU, CNR, CUT)

Imaging layered materials (LMU)

Bimodal AFM on Chlorite (Fig. 11) allows for a clear distinction between the two different layers of the mineral. While the contrast is already pronounced in common intermittent contact mode imaging, it is enhanced in the detection of the second eigenmode oscillation information. The results are summarized in Fig. 12. Figure 12a shows the topography of the cleaved chlorite surface, while (b) and (c) show the lateral contrast by the first eigenmode amplitude (d) and phase (e) signals, respectively. Using the mechanically driven second eigenmode simultaneously, amplitude and phase contrasts are strongly enhanced. It is strikingly that layers of the same material have the same contrast. Thus, the brucite-like and the T-O-T layers can be identified. When interpreting these data, we have to keep in mind that the two different layers are also differently charged. Thus, the strong contrast between the different materials may be mainly attributed to the charge differences.

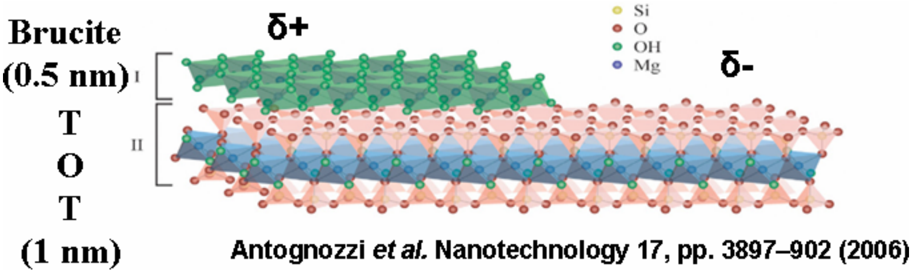

Antognozzi *et al.* Nanotechnology 17, pp. 3897–902 (2006)

Figure 11 Structure of chlorite.

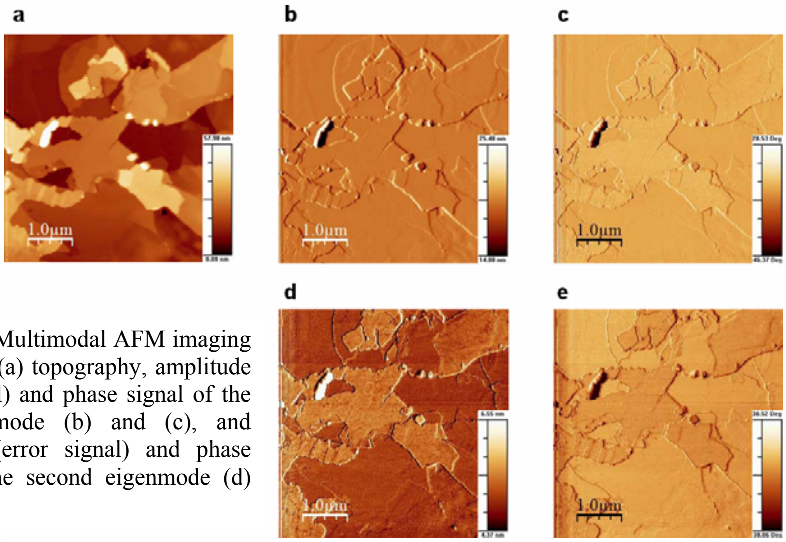

Figure 12. Multimodal AFM imaging of chlorite. (a) topography, amplitude (error signal) and phase signal of the first eigenmode (b) and (c), and amplitude (error signal) and phase signal of the second eigenmode (d) and (e).

Imaging antibodies (CSIC)

The general character of the method as well as the spatial resolution of bi-modal AFM in air are characterized by imaging biomolecules (single antibodies)**.** Antibodies are proteins that have well defined structures and binding sites which makes them good candidates to test the sensitivity and resolution of the bi-modal AFM for biomolecular imaging. First, we have imaged small and flexible IgG antibodies deposited on mica (Fig. 13). IgG is a Y-shaped protein that consist of four polypeptide chains arranged in three fragments, one Fc receptor and two identical Fab antigen-binding sites (Fig. 13*c*). The van der Waals length of each fragment is about 6.5 nm. Because of the flexibility of IgG, the antibody adopts several morphologies and in particular the Y shape (Fig. 13b). The cross-section along the lines depicted in Fig. 13b allows us to identify the position of the Fc and Fab fragments. Two of the fragments show the same phase shift of 5° while the third fragment shows a phase shift peak at 8° (Fig. 13d).

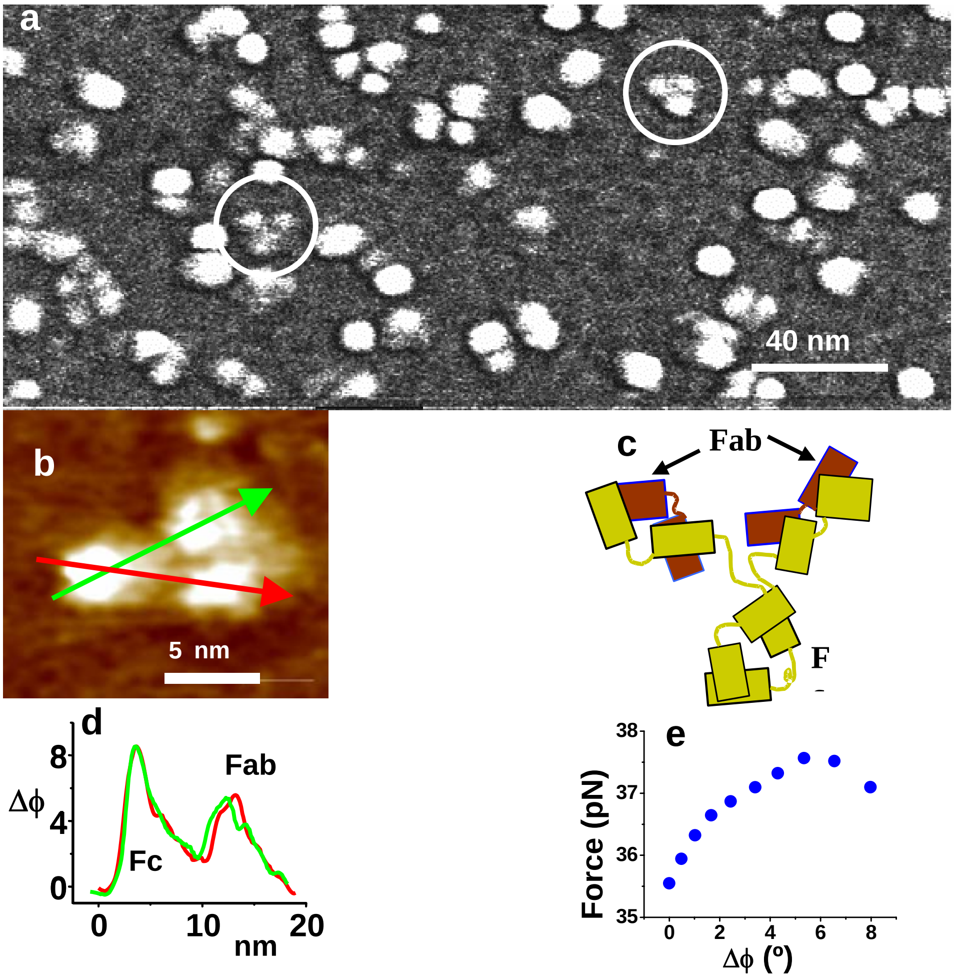

Figure 13. (a) Bi-modal AFM image of a region of a mica surface with physisorbed IgG monomers. (b) Image of an individual antibody. (c), Schematic of the tertiary structure of IgG molecules. The heavy chain are in green and the light chains in red. (d) Phase shift cross sections along the arrows depicted in Fig. 29b. (e) Calculated maximum force per cycle along the phase shift cross-sections shown in Fig. 29c. A_{01}=6 nm, A_{02}=0.5 nm, R=5 nm, f_1=119.4 kHz and f_2=749.3 kHz.

Similar results have been obtained with other IgG molecules. Consequently, we assign the larger peak to the Fc fragment and the smaller peaks to the Fab fragments. This result shows that the identification of different components along the protein chains is possible by the present method.

A direct comparison between amplitude modulation (tapping mode) and bi-modal AFM images illustrates some of the advantages of the latter for high resolution imaging of isolated biomolecules under the application of very small forces. To assure a meaningful comparison, we have used an AFM that enables to perform both amplitude modulation and bi-modal AFM imaging. Figures 30*a* and 30*b* show tapping mode topography and phase shift image of an IgM antibody. IgM has five Ig monomers, each of them having one Fc and two Fab fragments. Additionally, there is a small polypeptide chain (J-chain) joining two consecutive Fc fragments.

The image was obtained by applying a maximum tip-molecule force below 100 pN. The small value of the force explains the lack of contrast in both amplitude modulation AFM images (see discussion below). Fig. 14*c* shows the bi-modal AFM image obtained along with Fig. 14*a*-*b*. The bi-modal AFM image shows the five Ig monomers as well as the J-chain. Similar have been obtained by imaging IgG molecules. Tapping mode AFM images of a single IgG in both topography and phase shift (Fig. 14*d* and *e*) show a featureless and faint object while the bi-modal AFM image resolves the Fab and Fc fragments of the protein (Fig. 14*f*).

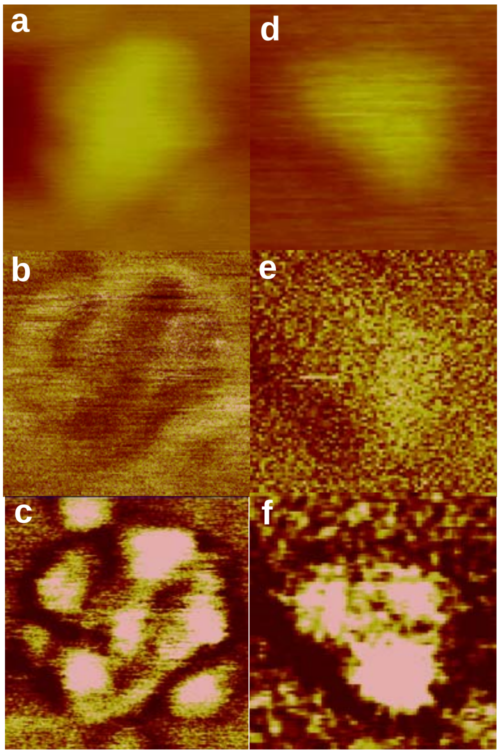

Figure 14. (a) Amplitude modulation AFM image (tapping mode) of and IgM molecule (topography). (b) Amplitude modulation phase shift image of *a*. (c) Bi-modal AFM image of the same IgM pentamer. The image shows the five subunits surrounding and the central structure (J-chain). Figs. 30*a-c* have been obtained simultaneously. (d) Amplitude-modulation AFM topography image of an IgG molecule. (e) Phase shift image of *d.* (f) Bi-modal AFM image of the same IgG monomer. The image reveals the presence of Fab and Fc fragments. Fig. 30 *d*, *e* and *f* have been obtained simultaneously.

Bimodal AFM imaging of antibodies in water (CSIC)

In this period we have applied the bi-modal AFM system to image IgG and IgM antibodies in water. Bimodal imaging AFM in water is more hard than in air because of the difficulty to find the eigenmodes. Here we have located the eigenmodes in liquids by analyzing the thermal noise spectrum of the cantilever.

The experiments are performed with the bi-modal AFM that enables the simultaneous excitation of the first and second resonances of the microcantilever beam. The *rms* amplitude of the first mode is fed back to the controller for topography imaging while the phase shift of first and second mode are recorded and plotted to detect compositional variations. Phase shift measurements are performed with doped n^+-type silicon cantilevers with a nominal radius of 10 nm (Nanosensors, Germany).

Figure 15 shows the bimodal AFM image (ϕ_2) of several antibodies molecules on mica. The experiment was performed with free amplitudes of A_{01}=6.9 nm and A_{02} =1.4 nm for first and second mode respectively. The set point amplitude was established at 6.0 nm. The relatively low resolution image (Fig. 15a) shows several antibodies deposited on the mica surface. Within the molecule several domains can be spotted. The higher resolution phase image (Fig. 15b) reveals the position of the different monomers and the J-chain. The comparison with the topographic image obtained simultaneously with the phase shift reveals no information about the domain structure of the IgM (Fig. 15c).

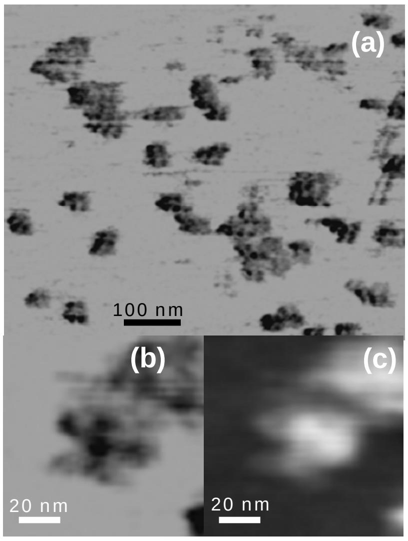

Figure 15. (a) Bimodal AFM image of several IgM antibodies on mica in water. (b). Bimodal AFM image of a single IgM antibody. The monomers and the J-chain are resolved. (c). Topography of the same antibody. The topography does not reveal the domain structure of the IgM.

Combination of nanotomography and bimodal AFM imaging (CUT, LMU)

We have demonstrated the compatibility of bimodal AFM imaging with Nanotomography imaging of heterogeneous polymers. In this way Bimodal AFM could be applied to render three dimensional images. The bimodal concept was applied to image elatomeric polypropylene (ePP) where the first two flexural eigenmodes of the cantilever are mechanically excited and the cantilever deflection signal is analyzed using two lock-in amplifiers realized by the bimodal control unit (CSIC, Eldisa). While the amplitude of the first mode is used as an electronic feedback signal, the amplitude and phase signal of the second eigenmode are used to distinguish compositional changes of the material. We used SEIHR-SPL cantilever (Nanosensors, Germany) ($f_1 \approx 122$ kHz, $f_2 \approx 758$ kHz), a free amplitude A_0 of about 30 nm and an amplitude ratio between the two modes of $A_2/A_1 = 0.2$ which turned out to fit best for the specific polymer and the particular application. We removed thin layers of ~ 10 nm thickness of the polymer by wet-chemical etching by applying a solution of 50 mg/ml potassium permanganate in 30 wt.-% sulfuric acid for one minute. After rinsing the specimen with 10 wt.-% sulfuric acid the etching was stopped by flushing with hydrogen peroxide, cleaned with pure water and dried with acetone. The etched sample was remounted into the AFM and the position of interest was retrieved by pre-alignment using an optical microscope and successively decreasing the image scan size, beginning with 10 µm towards 1 µm. After data acquisition the obtained stack of images was post processed including flattening and filtering and then combined to a volume image like in previous studies. The visualization has been done with AMIRA® (Mercury™ Computer Systems Inc., USA).

Figure 16 shows a comparison between the phase images of the fundamental resonance (a) and the second eigenmode (b) with bimodal excitation after one etching step. Dividing the average phase value of all data points within one image by its standard deviation exhibits clearly the higher signal to noise ratio for the second eigenmode phase images compared to the cantilever's fundamental eigenmode. This particular feature is valid for the whole image sequence except the very first captured image, i.e., before starting ablating. This might be caused by the prevailing thin layer of amorphous phase with lower surface energy at the surface of the specimen. In this case the motion of the cantilever's second eigenmode hardly senses compositional contrast of the specimen in layers directly beneath the surface. Comparing the images of the etching sequence

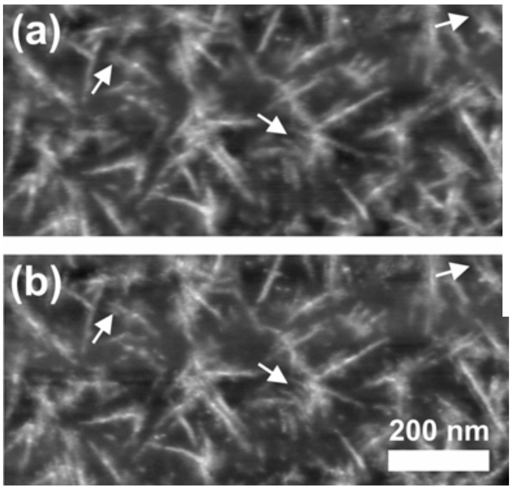

Figure 16. Comparison of phase images of the first eigenmode (a) and the second eigenmode (b) after one etching step at the same position of the ePP specimen. An amplitude ratio of $A_1/A_2 \approx 0.2$ was chosen for all measurements. Qualitatively, the structure corresponding to the cantilever's first eigenmode appears blurred in contrast to the second eigenmode. The phase signal of the second eigenmode is less noisy and shows the structure in more detail. In case of the first mode phase image crystallites can hardly be distinguished at positions indicated by the white arrows.

obtained with the two different resonance modes the phase image corresponding to the first eigenmode appears always a bit more blurred compared to the second eigenmode phase image which shows more sharply defined features (Fig. 16). The white arrows in Fig. 16 indicate positions where two or more crystallites can hardly be distinguished in case of the first eigenmode phase image but are clearly visible in the second eigenmode image. This effect is seen in all images of our etching series (except for the images taken before etching) which is a great advantage for nanotomography imaging.

The resulting nanotomography volume image prepared from the measured stack of images is shown in Fig. 17. To benefit from the mentioned advantages of the bimodal concept the phase values of the 2nd eigenmode was used and combined with the height data to accomplish a volume image of ePP. For clarity only the crystalline polymer phase is displayed.

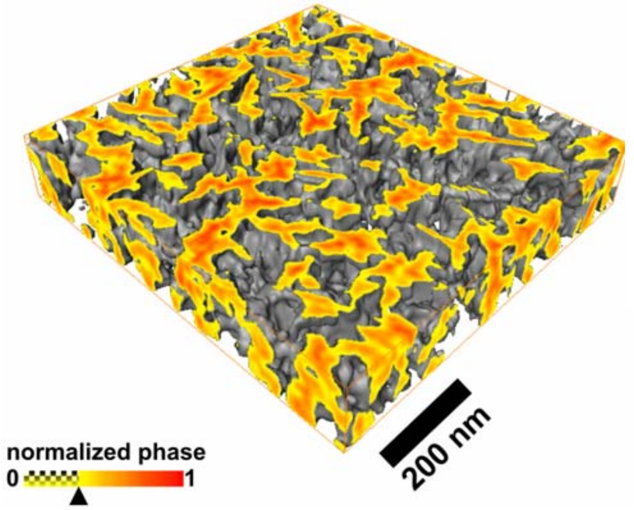

Figure 17. Nanotomography image (512 × 512 × 14 voxels) of ePP. The image was captured using bimodal imaging and the topography measured together with the 2nd eigenmode phase signal. The threshold to distinguish between amorphous and crystalline phase was set to 0.32 (see marker at the colorbar). The boundary box faces were colored according to the corresponding phase values.

Multimaterial Methodology

The ***multimaterial methodology*** will allow to transform the amplitude, frequency or phase shift changes measured by the instrument into quantitative information about the sample properties. The multimaterial methodology has both a ***general framework*** to describe dynamic force microscopy interactions and ***specific codes*** to be used with different materials such as inorganic materials, biomolecules, polymers or molecular architectures.

Composition identification by dynamic force microscopy methods (CSIC, JKU, CNR, UT, CUT)

Ordered phase separated surfaces (UT)

We have used dendrimers as convenient samples to test the use of the AFM to determine some mechanical properties at the nanoscale such as the Young modulus. Dendrimers are branched molecules that can be synthesized in different sizes, usually in the 1-5 nm range. Separated single dendrimers have been obtained by using spin coating or soft lithographic stamping. The discrimination between dendrimer aggregates and single dendrimer macromolecules can be made through the characteristic size of the features. The main outcome of this is that we are able to determine *qualitatively* the difference in mechanical properties between patterned and unpatterned substrates. This sample preparation was achieved by spin coating. Using this method, one can obtain single dendrimers (G5-PAMAM, generation 5 poly(amidoamine)) deposited on silicon substrates with a surface concentration of one dendrimer/μm^2. Such a low concentration is suitable to perform nanomechanical experiments on dendrimers. Single dendrimers can be identified by their height and diameter. The dendrimers form stacks on silicon substrate with equal height difference between consecutive layers.

The nanomechanical properties of single dendritic macromolecules were probed by measuring force versus distance curves in the compression mode. Figure 18 shows force-distance curves taken at different positions on the sample. In comparison to the linear relationship between the load and compression on the silicon substrate, indentation of dendrimers display a remarkable nonlinear response when compressing the dendrimers with the AFM tip. For G5 PAMAM dendrimers, the indentation (compression) increases nonlinearly with applied load. The maximum indentation depth was about 1.2 nm. This value is comparable to the size of individual dendrimers. Clearly the substrate was much harder to penetrate. This is reflected by the steep increase of the force as a function of indentation. On the other hand, the nonlinear relationship between load and indentation for the dendrimers is typical for soft deformable materials. The force-compression curves for the dendrimers show also a steep increase of the slope of the curve at higher indentations. This is due to the influence of the hard silicon substrate under the dendrimers. To obtain the value of the modulus we transform the force-indentation curves into log(F)-log(h) plots. If the Hertz model holds for the investigated samples, such plots should be linear and have a slope equal to 3/2:

$$\log F = \frac{3}{2}\log h + \log\left(\frac{4E\sqrt{R}}{3(1-\nu^2)}\right) \qquad (2)$$

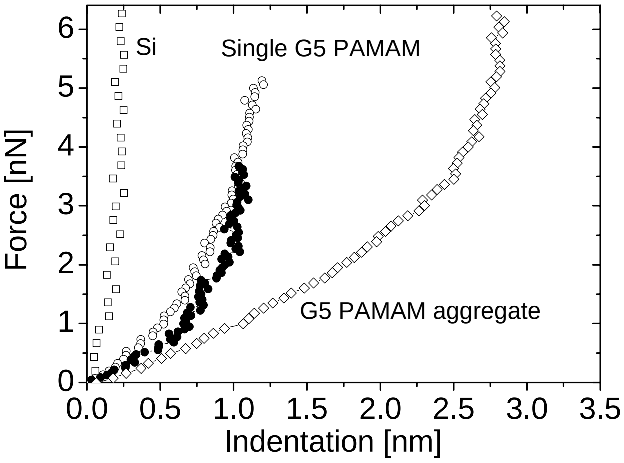

Figure 18. Force-compression curves for single dendrimers, dendrimer aggregates, and silicon substrate.

Phase-spectroscopy (CSIC, CUT, UAM, CNR)

Transformation between phase shifts and energy dissipation

In the ForceTool project we have pursued the use of the phase shift between the mechanical exciation of the cantilever and its response as a means to extract information about the sample’s properties with nanoscale spatial resolution. We have developed a method to identify the mechanism of energy dissipation at the nanoscale. The method requires the determination of the energy dissipated on the sample surface as a function of the oscillation amplitude while the tip approaches the surface. The representation of the dissipated energy and, in particular, its derivative with respect to the amplitude, dynamic-dissipation curves hereafter, characterizes the dissipation process. Three different nonconservative processes are studied: surface energy hysteresis, viscoelasticity and long-range dissipative interfacial interactions. We have performed both simulations and experiments. The quantitative and qualitative agreement obtained between calculations and experiments performed on silicon and polystyrene samples supports the validity of the identification method proposed here.

We have used a point-mass model to calculate the properties and interactions of a vibrating tip in the proximity of a surface, and to establish the relationships between experimental observables and material properties. Let's consider the steady state of a vibrating tip that interacts with the sample surface through conservative (short and long-range forces) and nonconservative interactions. Then, the energy per cycle supplied by the external force (E_{ext}) must be converted into either hydrodynamic damping in the medium (E_{med}) or energy dissipated in the sample (E_{dis}). Furthermore, in many situations of interest, the tip motion can be described by a sinusoidal function $z=z_0+A\cos(\omega t-\phi)$. Those assumptions allow us to express the energy dissipated (per cycle) on the sample surface in terms of experimental quantities,

$$E_{dis} = E_{ext} - E_{med} = \frac{\pi k A}{Q}\left(A_0 \sin\phi - \frac{A\omega}{\omega_0} \right) \tag{3}$$

where E_{med} is modelled by a linear viscous damping law ($F_{med}=-b\dot{z}$); Q is the quality factor of the cantilever; A_0 is the amplitude very far from the surface and Φ is the phase shift between the external excitation and the tip response.

The sample deformation and its associated stress is calculated by the Derjaguin, Muller and Toporov model, i.e.,

$$F_{DMT} = Y^* R^{1/2}\delta^{3/2} - 4\pi R\gamma \tag{4}$$

then the energy dissipated by surface energy hysteresis processes can be calculated by,

$$E_{dis} = \oint F_{DMT}\,dz = 4\pi R\delta(\gamma_r - \gamma_a) \tag{5}$$

Where δ is the deformation (indentation) and F_{DMT} is the DMT forces in approach and retraction half periods; γ_r and γ_a are respectively the approach and retraction surface energies and Y^* is the effective elastic modulus of the interface and R is the tip radius. Long-range dissipative interfacial forces, i.e., interactions that do not imply the mechanical contact between probe and surface (non-contact) can be calculated by using a time-dependent power law interaction where the strength of the force α depends on whether the probe approaches (α_a) or retracts away (α_r) from the surface. Its deduction will not be shown here, although an expression for the dissipated energy in terms of the strength of the interaction force can also be deduced..

The viscoelastic behaviour is calculated by using the Voigt model and by assuming that the contact area and sample deformation are calculated by the Hertz. The above assumptions give a time dependent viscous force as ,

$$F_v = \eta\sqrt{R\delta}\,\frac{d\delta}{dt} \tag{6}$$

where η is the viscosity.

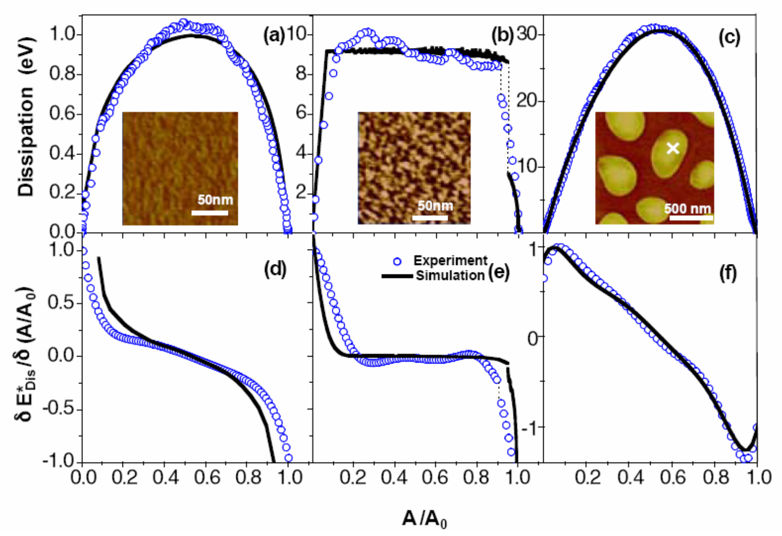

Figure 19. Measured and simulated dynamic dissipation curves: (a) on Si without mechanical contact between tip and surface.(b) on Si with surface energy hysteresis and long-range interfacial interactions. (c) on a PS region of a PS/PB blend. d-f, Derivatives of the normalized energy-dissipation curves shown in **a** and **c**, respectively

The amplitude and phase shift dependencies of the oscillation on tip-sample separation were obtained by approaching the tip towards the sample from a distance with negligible tip-sample interaction. The curves were taken at 2 Hz. Then, Eq. (3) was used to turn data into dissipation values.

In Figure 19 we provide a comparison between theory and experiments performed on silicon and on a polystyrene (PS) region of a blend of polystyrene-polybutadiene (PS/PB) polymer. The experimental dynamic-dissipation curves reproduce the behaviour predicted by the theory. Energy-dissipation curves for long-range interactions and viscoelasticity may look similar (Figs. 19a and 19c, but the derivative unambiguously singles out each dissipative process (Figs. 19d-f). The simulations presented in Figs. 19b and 19e, consider both long-range dissipative interactions and surface energy hysteresis because the experimental data shows both dissipation in the attractive and repulsive regimes of the AM-AFM. The step-like discontinuities observed in Fig. 19b mark the transition between attractive and repulsive regimes (discontinuous line).

Molecular dissipation mechanism in sexithiophene monolayers

We have combined experimental measurements of the energy transferred by a silicon dioxide tip into a region of sexithiophene molecules, with continuum modeling and first-principles calculations to identify the molecular processes responsible for the contrast observed in phase-imaging force microscopy (Fig. 20). First we have measured the energy transferred by a silicon dioxide tip into a region of sexithiophene molecules to be of 1.4 eV per cycle. Contact mechanics modeling established an effective interaction diameter of 2 nm which implies a dissipation of 0.18 eV per molecular chain. This value is comparable to the average value (0.15 eV) determined from first principle calculations for an indentation of 0.20 nm. Short-range dissipation contributions can be extracted from the dissipated energy versus oscillation amplitude curves taken in both the attractive and repulsive regimes with the aid of contact mechanics modeling. First-principles calculations show that the adhesion hysteresis observed experimentally has its molecular origin in the rich configuration space of the system. During the approach (loading) the system is trapped, due to the presence of energy barriers, in several bonding configurations that differ from those sampled in the retraction stage of the tip (uploading). Those configurations correspond to local energy minima. We have demonstrated that some of the energy detected in phase-imaging experiments performed in technological environments is directly related to the molecular properties of the material.

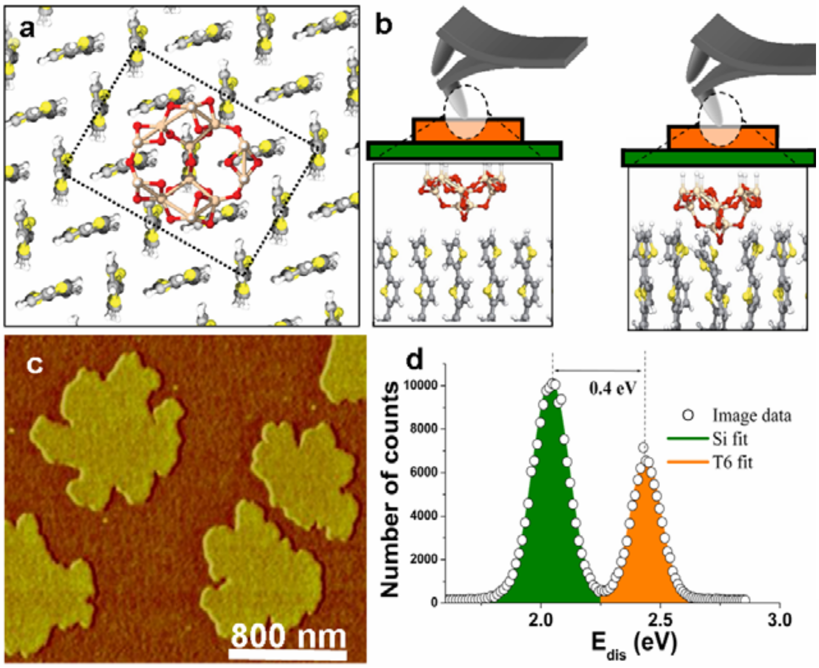

Figure 20. (a) Top view of the herringbone structure and unit cell of sexithiophene. A single silica tip stands on top of the molecules. (b) Schematic illustration of the tip-oligothiophene interface. It includes first-principle simulation of an interaction between a silica tip and a T6 molecule at two different distances. (c) Phase-imaging force microscopy images of several T6 monolayer islands deposited on silicon. (d) Energy dissipation histograms extracted from (c). The number of counts is larger on the silicon surface because at the present coverage its surface area is larger. Color code for the atoms: oxygen (red), sulfur (yellow), carbon (grey), hydrogen (white) and silicon (light salmon).

Nanoscale electrical properties (CNR)

In an effort to understand the dynamics of the tip-surface interaction under electrostatic interactions, we have studied the sensitivity and contrast in Kelvin probe force microscopy by applying an electrostatic force to the cantilever tuned at the first and second flexural frequencies. The measurements were performed on different test samples such as macroscopic electrodes, small nanocrystals and thin organic layers. To improve our comprehension of phase electrostatic contrast at higher harmonics, we used a multi-scale strategy performing measurements on samples with increasing morphology complexity starting from uniform substrates, then moving to mesoscopic structures, and finally performing potential measurements on nanometric objects such as inorganic nanostructures and organic thin films. An extensive range of samples and structures with sizes spanning from several microns down to a few nanometers and possessing different electrical behaviors have been studied. In particular, bulk materials such as Au and graphite (HOPG), thick and thin polymeric films of Poly(3,4-ethylenedioxythiophene) poly(styrenesulfonate) (PEDOT:PSS), Poly-3-hexylthiophene (P3HT) and Polyisocyanopeptides (PIC), as well as nanostructures of silicon oxide and SiC nanocrystals have been studied.

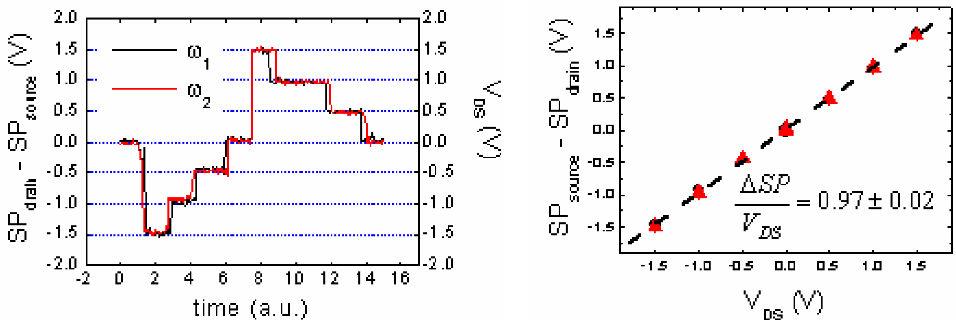

Figure 21. *Left*: potential difference measured between source and drain of a transistor by KPFM using first and second mode, while varying the applied potential. *Right:* SP difference between source and drain (ΔSP) measured by applying to the electrodes different potential drops (V_{DS}) and using 1st (black circle) and 2nd (red triangle) oscillation modes. Black line represents the linear fit of the two dataset; the angular coefficient is close to unit.

Macroscopic electrodes are used as test samples for the potential calibration of the microscope, in both oscillation modes, showing that the measured Surface Potential (SP) results equal to the applied potential drop and that the different working frequencies do not affect the measured potential.

The measured work function (WF) does not depend on the used oscillation frequencies of the cantilever. In the case of conductive materials the measured SP always correspond to the material WF. In more complex systems such as thick polymeric films, the measured WF falls nearly halfway in the HOMO – LUMO gap of the single monomer, as expected. All the measured values are collected in table 1. The table shows a good agreement with those values reported in literature.

Sample	**Surface Potential (mV)**		
	1st mode	2nd mode	literature
PIC	-200 ± 20	-230 ± 20	-200[1]
P3HT	-550 ± 30	-530 ± 30	-560[2]
PEDOT:PSS	190 ± 20	200 ± 20	160[3]
Au	210 ± 30	220 ± 30	190[4]

Table 1 – SP values obtained by KPFM measurements performed in two oscillating modes. The measured values are in good agreement with those reported in literature. The SP values are calculated respect to the HOPG value. [1] article in preparation, [2] Cascio AJ et al., Appl. Phys. Lett 88, 062104 (2006), [3] Shin WS et al., J. Mater. Chem. 16, 384 (2006), [4] Ashcroft N. W., Mermin N. D., *Solid State Physics*, Philadelphia.

In the case of Au, HOPG and conductive polymer (PEDOT:PSS), the measured SP in the two oscillation mode agree and the value is the same of the bulk value. Instead, for semi-conductive (P3HT) and insulating (PIC) film, potential variations are achieved using different oscillation modes. These differences can be ascribed to different polarization effects on the surface of the film, due to the oscillating charged tip with different frequencies.

By reducing the thickness of the samples to a few nm (i.e. Au, HOPG and polymeric films) excitation at first and second mode give a different behavior in the potential images. In this case, the definition of the measured SP is more complex respect to the bulk materials, and is given by different terms: WF, potential drop across the film, potential barrier at the film-substrate interface and surface due to dipoles, as well as polarization effects due to the charged tip.

High resolution imaging of biomolecules at higher harmonics (JKU)

The nonlinear character of the tip-surface forces gives rise to the excitation of higher harmonic components of the driving frequency ω. Those harmonics are multiples of the driving frequency $n\omega$. They are very prominent in liquids, where the quality factor of the cantilever is very low Q~1. We investigate the motion of a cantilever interacting with a sample under highly over-damped conditions in liquids. The nonlinearity of the interaction forces give rise to complex dynamics in the tip motion, which can be utilized to obtain information about the elastic properties of the sample. We show that for low quality factors Q, higher harmonics (i.e. integer multiples of the excitation frequency) significantly contribute to the motion. A point mass model was introduced to qualitatively explain the origin of these contributions and compared to experimental findings. The equation of motion of a cantilever tip immersed in liquid can be approximated by a one dimensional forced harmonic oscillator with damping, yielding the nonlinear, second order differential equation

$$m\ddot{x} + \frac{m\omega_0}{Q}\dot{x} + kx = F_0 \cos(\omega t) + F_{hyd}(d_{ts}) + F_{ts}(d_{ts}) \qquad . \qquad (7)$$

F_{ts} is the sum of an attractive van der Waals force and the repulsive force due to elastic interactions between the tip and the surface. Amplitude *versus* distance curves were simulated by numerically solving the equation of motion, Eq.(7). The simulated amplitude *vs.* distance curve is shown in Fig. 22a for a free amplitude of A_0=4 nm and a driving frequency f_d of 7.2 kHz. For comparison, Fig. 221b shows an experimental amplitude *vs.* distance curve obtained for the same A_0 and the same materials. At distances smaller than A_0 the tip senses the tip sample interaction forces, which leads to the characteristic amplitude decrease. In this region, energy is transferred into higher harmonics (i.e. integer multiples) of the cantilever angular frequency.

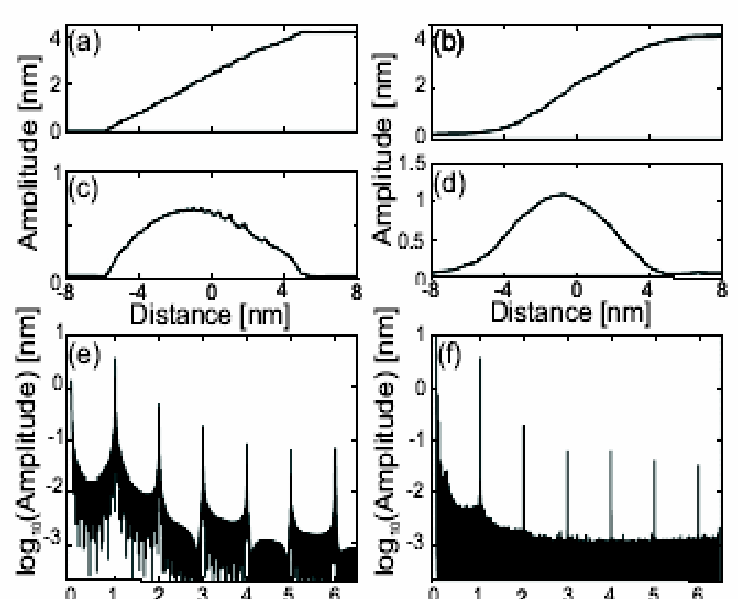

Figure 22. Comparison between simulation and experimental data obtained for a silicon nitride tip interacting with a mica surface in buffer solution. **(a)** Simulated amplitude vs. distance curve. **(b)** Measured amplitude vs. distance curve. **(c)** Simulated 2nd harmonic amplitude vs. distance curve. **(d)** Experimental 2nd harmonic amplitude vs. distance curve obtained using an external Lock-in amplifier. **(e)** Frequency spectra (normalized by the driving frequency) obtained from simulation for $A_{sp}/A_0=0.9$. **(f)** Measured frequency spectra (normalized by the driving frequency.

The contribution of the 2nd harmonic, A_2, is shown in Fig. 22c for the simulation and in Fig. 22d for the experiment. In both cases a qualitatively similar initial and final decrease of A_2 along the tip-sample distance can be observed. Interestingly, the 2nd harmonic amplitude was about one order of magnitude greater than the values reported from experiments performed in air.

The frequency spectra for a relative amplitude reduction $A_{sp}/A_0=0.9$ is shown in Figs. 22e-f, revealing good accordance between simulation and experiment. From the experimental spectra, an estimate for the measurement noise of ~ 3 pm can be given.

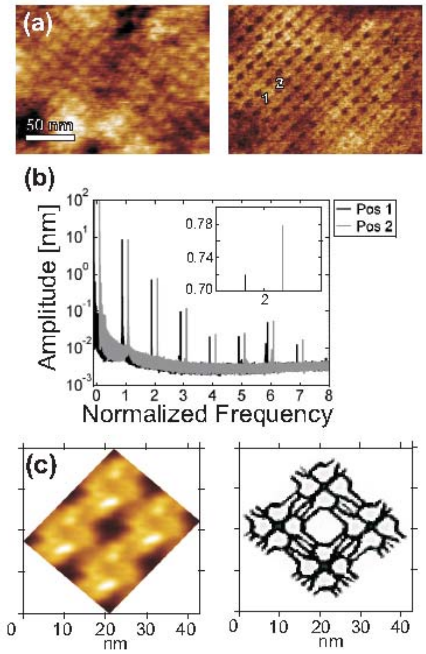

Figure 23. High resolution on a bacterial S-layer. 2nd harmonic images were recorded using an external Lock-in amplifier. **(a)** Simultaneous recorded topography (left panel) and 2nd harmonic image (right panel). Substructures within the unit cell can be clearly observed (resolution ~0.5 nm). Scan size: 210 x 175 nm^2; color code: 0-0.9 nm, 0-0.5 V. **(b)** Frequency spectra recorded on positions 1 and 2 of (a). The spectral contributions reflect the different properties of the tip-protein (pos. 2) and tip-hole (pos. 1) interactions (note that spectra are shifted with respect to the normalized driving frequency for better visibility). Inset: Contribution of the 2nd harmonic amplitude in linear representation. **(c)** Average of 55 unit cells (left panel) from (a, right panel) and a sketch of the expected lattice structure (right panel).

To verify the potential of this method, 2nd harmonic amplitude and topography images were simultaneously recorded on the surface of S-layer rSbpA-*strep*-tagII recrystallized on cleaned silicon (A_0~10 nm, $A_{sp}/A_0=0.85$, f_d= 7.3 kHz, k=0.1 N/m, BPS buffer). The topography image [Fig. 23 (a), left panel] reveals a lattice with p4 symmetry and a periodicity of ~14 nm, which is in agreement with the structure known from literature. In addition to this, the 2nd harmonic image [Fig. 23 (a), right panel] shows detailed substructures within the unit cell of the S-layer. Even at areas where the topographical image is blurred due to the underlying roughness of the silicon surface, the 2nd harmonic image clearly resolves the local properties of the protein lattice. Frequency spectra were recorded on two distinct positions of the sample. They are marked in Fig. 23 (a). The spectra shows the harmonic contributions to the tip motion [Fig. 23 (b)] at a hole (position 1) and at the position occupied by a protein (position 2) (note that the amplitude scale is logarithmic and the spectra are shifted with respect to the normalized driving frequency for better visibility). The corresponding 2nd harmonic amplitude values of 0.72

(position 1) and 0.78 nm (position 2) yielded a difference (60 pm) well above the noise level (~3 pm). In accordance with the simulations different harmonic contributions were observed in the whole frequency range reflecting the underlying variation of the tip-sample interaction. The strong dependence of the 2nd harmonic amplitude on elasticity differences can be attributed to the significant amount of energy transferred from the driving frequency to its 2nd harmonic, when nonlinear tip-sample interaction occur in a highly over-damped system. The enhanced lateral resolution arising from this effect is demonstrated in Fig. 23 (c). An average of 55 unit cells (left panel) of the 2nd harmonic image [Fig. 23 (a), right panel] clearly reveals the structure known from literature, Fig.23 (c) right panel.

Second harmonic amplitude images were also recorded from human rhinovirus serotype 2 (HRV2). The virus is bonded by electrostatic interactions to a clean mica surface (A_0~15 nm, A_{sp}/A_0=0.9, f_d= 7.9 kHz, k=0.1 N/m, Ni-Tris buffer). A fairly dense layer of the virus (spherical shape, diameter ~ 30 nm) can be observed in the topography image [Fig. 24(a)], whereas the 2nd harmonic amplitude image reveals details of the capsid structure (circle) of the virus [Fig. 24(b)]. These substructures might reflect the protrusions on the surface of the viral capsid known from cryo-EM and X-ray imaging. These examples demonstrate that mapping higher harmonics of the cantilever motion under highly over-damped conditions in liquids provides additional information on the sample properties, since the sensitivity of these higher harmonic amplitudes is strongly enhanced compared to the operation in air.

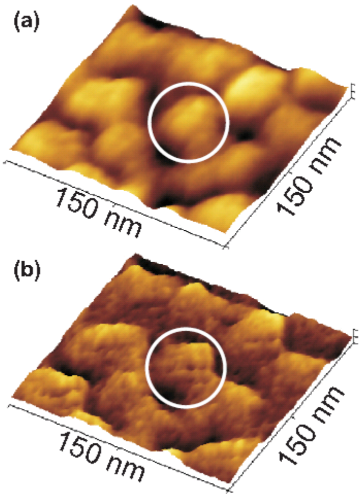

Figure 24. Measurements on human rhinovirus serotype. **(a)** Topography image of HRV2 layer on mica. **(b)** Simultaneously recorded 2nd harmonic amplitude image clearly revealing substructures of the viral capsids (circle). Scan size: 350 x 350 nm^2; color code: 0-13 nm, 0-0.35 V.

References

- J.R. Lozano and R. Garcia, Theory of multifrequency AFM, *Phys. Rev. Lett.* **100**, 076102 (2008) .
- M. Bauer, A.M. Gigler, C. Richter, R.W. Stark: "Visualizing stress in silicon microcantilevers using scanning confocal Raman spectroscopy", *Microelectron. Eng.*, in press
- S. Patil, N.F. Martinez, J.R. Lozano, R. Garcia, Force microscopy imaging of individual protein molecules with femto Newton force sensitivity, *J. Mol. Recog.* ***20,*** 516-523 (2007)
- J. Preiner, J. Tang, V. Pastushenko, and P. hinterdorfer, Higher harmonic AFM: Imaging of biological membranes in liquid, *Phys. Rev. Lett.* **99**, 046102 (2007).
- R. Garcia, R. Magerle, R. Perez , Nanoscale imaging with gentle forces, *Nature Materials* **6**, 405 (2007)
- R. Vázquez, F.J. Rubio-Sierra, R.W. Stark, Multimodal analysis of force spectroscopy based on a transfer function study of micro-cantilevers, *Nanotechnology*, **18**, 185504 (2007)
- R. W. Stark, N. Naujoks, A. Stemmer, Multifrequency electrostatic force microscopy in the repulsive regime, *Nanotechnology* **18**, 065502 (2007)
- F. J. Rubio-Sierra, R. Vazquez,and R. W. Stark, "Transfer Function Analysis of the Micro Cantilever used in Atomic Force Microscopy", *IEEE T. Nanotechnology* **5**, 692-700 (2006)
- R. Garcia, C.J. Gomez, N.F. Martinez, S. Patil, C. Dietz, R. Magerle*,* Identification of nanoscale dissipation processes by dynamic atomic force microscopy, *Phys. Rev. Lett.* **97**, 016103 (2006).
- N.F. Martinez, S. Patil, J.R. Lozano and R. Garcia*,* Enhanced compositional sensitivity in AFM by the excitation of the first two flexural modes, *Appl. Phys. Lett.* **89**, 153115 (2006).
- N.F. Martinez and R. Garcia*,* Measuring phase shifts and energy dissipation with amplitude modulation AFM, *Nanotechnology* **17**, S167 (2006).

Section 1- Exploitable knowledge and its Use

Exploitable Knowledge	**Exploitable product**	**Sector**	**Timetable for commercial use**	**Patent s**	**Owner and Other partners involved**
1. Bi-modal AFM operation	AFM microscope	1. Microscopy 2. Nanotechn.	Under commercial use	Two PCT patents have been filed	CSIC
2. Cantilevers for bi-modal AFM operation in liquids	Silicon microcantilevers	1. Force microscopy	2008-2008	A patent is planned for 2008	NanoWorld Services

Bi-modal AFM concept. New concept of operation of an atomic force microscope**.** The *bi-modal AFM concept* considers the cantilever as a three dimensional object with several resonance modes, in particular two. The double excitation allows to separate topography from composition contributions in the experimental data. Furthermore, computer simulations show that the bi-modal AFM is about two orders of magnitude more sensitive to force variations than state of the art tapping mode AFMs. The concept was developed by CSIC scientists.

Intellectual Property Rights: Patents filed: WO 2008/003796 and WO 2007/036591

Contacts have been established with some companies interested in AFM development (air or liquids) such as Asylum Research (USA), Nanotec (Spain) and ScienTec (France). In July 2007 Asylum Research (USA) has acquired the rights to commercialize the CSIC patents on the bi-modal AFM concepts. The product is already available in the market (www.asylumresearch.com).

Bi-modal AFM cantilevers for operation liquids. Nanoworld services has designed a cantilever with a geometry suitable to amplify the second eigenmode in liquids.

Intellectual Property Rights: A patent application is underway.

Section 2-Dissemination of Knowledge

Overview table

Planned/actual dates	Type	Type of Audience	Countries	Size of Audience	Partner responsible/Involved
11.08.2007	Report, Oberösterreichische Nachrichten (daily newspaper)	All	Austria		JKU
5 June 2007	Radio, COPE	All	Spain		CSIC
4 June 2007, broadcast 19-20 horas	Radio, Onda Regional de Murcia	All	Spain		CSIC
July 2007	Report, Journal, EL PAIS	All	Spain		CSIC
26-30 November 2007	MRS 2007 Fall Meeting	Research	All	200	CSIC
1-2 October 2007.	Second International Symposium on Atomic Technology (ISAT-2). Awaji (Japon)	Research			UAM
September 27, 2007	SPM and organic materials, Hamburg	Research	All		JKU
14 July 2007	ISPM 2007 Jeju, Korea	Research	All	200	JKU
Santa Margherita di Pula, Sardinia (Italy), 13 - 16 May 2007	VI ESF-Nanotribology Workshop	Research	EU	100	UAM
26.03.2007 – 30.03.2007	DPG “AKF-Frühjahrstagung 2007” in Regensburg	Research	All		CUT
21-22 June 2007.	Congreso Ibérico de Tribología, Bilbao (Spain)	Research	All	100	CSIC
31st May 2007	IRC workshop on nanoscale characterization, Bristol (U.K.)	Research	All	50	CSIC
19-21 April 2007	AFM BioMed Conference, , Barcelona	Research	All	250	CSIC,JKU, LMU
3-6, 2007 Linz, Austria	IX Annual Linz Winter Workshop, Feb.	Research	All	250	CSIC,CUT, LMU
7-9th December 2006, Atagawa, Japan.	14th International colloquium on scanning probe microscopy (ICSPM-14), 7-9th December 2006, Atagawa, Japan.	Research	Asia	200	CSIC
October 4-6 (2006), West Lafayette, Indiana, USA	Frontiers in Scanning Probe Microscopy,	Research	All	~150	LMU
October 4-6 (2006),	Frontiers in	Research	All	~150	CSIC

West Lafayette, Indiana, USA	Scanning Probe Microscopy,				
Osaka (Japan), 20 - 22 November 2006.	Handai Nanoscience and Nanotechnology International Symposium	Research	All		UAM
September 2006	32nd Int. Conf. on Micro- and Nanoengineering, MNE, Barcelona, Spain,	Research	All		LMU
2/08/2006	International Conference on Nanoscience and Technology (NANO9 meets STM06 in Basel)	Research	All	5~00	UAM, CSIC, LMU
19/07/2006	9th International Conference on Non-contact Atomic Force Microscopy	Research	All		UAM
3-6 (2006), Montpellier, France.	SPM 2006 Conference, June	Research	All	150	CSIC, JKU, LMU, UT
01/06/2006	E-MRS Spring Meeting, Nice (France),	Research	All		CNR
20/2/2006	Biophysical Society Meeting	Research	All		JKU
3/02/06	Conference Linz (Austria)	Research	EU	250	CSIC
3/02/06	Conference Linz (Austria)	Research	EU	250	UT, CNR, CUT, UAM,JKU
19/09/05	Conference	Research	EU		JKU
4/07/05	Conference STM 2005	Research	All		LMU
16/08/05	Conference, NC-AFM 2005	Research	All	150	CSIC
June 05	ECME05	Research	All	300	CNR
	Publication	Phys. Rev. Lett., **100**, 076102 (2008)	All		CSIC
	Publication	J. Am. Chem. Soc., **130**, 780-781(2008).	All		CNR
	Publication	Phys. Rev. Lett., **99**, 046102 (2007)	All		JKU
	Publication	Advanced Functional Materials **17**, 3791 (2007).	All		CNR
	Publication	J. Am. Chem. Soc.**,** **129**, 6477 (2007).	All		CNR
	Publication	Nature Mater. **6**, 405 (2007)	all		CSIC-CUT-UAM
	Publication	Small, **3**, 161 (2007)	all		CNR
	Publication	Rev. Scientific Instrum. 78,	all		CUT

		053703 (2007)			
	Publication	Phys. Rev. Lett., **98,** 106104 (2007)			UAM
	Publication	Nature **446**, 64 (2007)	All		UAM
	Publication	Nanotechnology, **18**, 185504, 2007	All		LMU
	Publication	Nanotechnology, **18**, 065502, 2007	All		LMU
	Publication	IEEE T. Nanotechnology, vol. 5(6), 692-700, 2006	All		LMU
	Publication	Phys. Rev. Lett. **97**, 016103 (2006)	All		CSIC, CUT
	Publication	ChemPhysChem **7**, 847 (2006)	All		CNR
	Publication	Adv. Materials **18**, 145 (2006)	all		CNR
	Publication	Adv. Functional Materials **16** 1407 (2006)	all		CNR
	Publication	Phys. Rev. Lett. **96**,106101(2006)	all		UAM
	Publication	Nanotechnology **17**, S167 (2006)	all		CSIC
	Publication	Appl. Phys. Lett. **89**, 153115 (2006)	all		CSIC

Section 3-Publishable results

3.1 Patent Applications

- Método de utilización de un microscopio de fuerzas atómicas y microscopio, R. García and Tomás R. Rodríguez, *PCT/ES2006/070016*

- Método para aumentar la sensibilidad de sistemas micro y nanomecánicos con excitación multimodal, R. Garcia, J.R. Lozano, N.F. Martinez, S. Patil, *PCT/ES2006/070096*

- C. Richter, T. Sulzbach, Bi-modal cantilevers with pronounced higher eigenmode and non-integer ratio between the frequencies of the first fundamental eigenmode and the pronounced eigenmode, *NanoWorld services GmbH* (in preparation).

3.2 Peer Review Publications

a). FT direct

- J.R. Lozano and R. Garcia, Theory of multifrequency AFM, *Phys. Rev. Lett.* **100**, 076102 (2008) .
- M. Bauer, A.M. Gigler, C. Richter, R.W. Stark: "Visualizing stress in silicon microcantilevers using scanning confocal Raman spectroscopy", *Microelectron. Eng.*, in press
- S. Patil, N.F. Martinez, J.R. Lozano, R. Garcia, Force microscopy imaging of individual protein molecules with femto Newton force sensitivity, *J. Mol. Recog.* ***20,*** 516-523 (2007)
- J. Preiner, J. Tang, V. Pastushenko, and P. hinterdorfer, Higher harmonic AFM: Imaging of biological membranes in liquid, *Phys. Rev. Lett.* **99**, 046102 (2007).
- R. Garcia, R. Magerle, R. Perez , Nanoscale imaging with gentle forces, *Nature Materials* **6**, 405 (2007)
- R. Vázquez, F.J. Rubio-Sierra, R.W. Stark, Multimodal analysis of force spectroscopy based on a transfer function study of micro-cantilevers, *Nanotechnology*, **18**, 185504 (2007)
- R. W. Stark, N. Naujoks, A. Stemmer, Multifrequency electrostatic force microscopy in the repulsive regime, *Nanotechnology* **18**, 065502 (2007)
- F. J. Rubio-Sierra, R. Vazquez,and R. W. Stark, "Transfer Function Analysis of the Micro Cantilever used in Atomic Force Microscopy", *IEEE T. Nanotechnology* **5**, 692-700 (2006)
- R. Garcia, C.J. Gomez, N.F. Martinez, S. Patil, C. Dietz, R. Magerle, Identification of nanoscale dissipation processes by dynamic atomic force microscopy, *Phys. Rev. Lett.* **97**, 016103 (2006).
- N.F. Martinez, S. Patil, J.R. Lozano and R. Garcia, Enhanced compositional sensitivity in AFM by the excitation of the first two flexural modes, *Appl. Phys. Lett.* **89**, 153115 (2006).
- N.F. Martinez and R. Garcia, Measuring phase shifts and energy dissipation with amplitude modulation AFM, *Nanotechnology* **17**, S167 (2006).

b). FT related

- V. Palermo, A. Liscio, M. Palma, M. Surin, R. Lazzaroni, P. Samori, *Chemical Communications*, 3326 (2007).
- G. De Luca, A. Liscio, P. Maccagnani, F. Nolde, V. Palermo, K. Mullen, P. Samori, *Advanced Functional Materials* **17**, 3791 (2007).
- P. Stoliar, R. Kshirsagar, M. Massi, P. Annibale, C. Albonetti, D. M. de Leeuw, F. Biscarini, *Journal of the American Chemical Society* **129**, 6477 (2007).

•A. Liscio, G. De Luca, F. Nolde, V. Palermo, K. Müllen, P. Samorì, *J. Am. Chem. Soc.* **130**, 780-781 (2008).

•J.M. Mativetsky, M. Palma, P. Samorì* "Exploring Electronic Transport in Molecular Junctions by Conducting Atomic Force Microscopy", *Topics in Current Chemistry* **2008**

•A. Liscio, V. Palermo, P. Samorì "Probing local surface potential of quasi-one-dimensional systems: a KPFM study of P3HT nanofibers", *Adv. Funct. Mater.*, **2008** in print

• C. Dietz, S. Röper, S. Scherdel, A. Bernstein, N. Rehse, and R. Magerle, Automatization of nanotomography, *Review of Scientific Instruments* **78**, 053703 (2007)

.• Yoshiaki Sugimoto, Pavel Jelinek, Pablo Pou, Masayuki Abe, Seizo Morita, Rubén Pérez, and Oscar Custance, Mechanism for Room-Temperature Single-Atom Lateral Manipulations on Semiconductors using Dynamic Force Microscopy, *Phys. Rev. Lett.* **98**, 106104 (2007)

•Yoshiaki Sugimoto, Pablo Pou, Masayuki Abe, Pavel Jelinek, Rubén Pérez, Seizo Morita, and Oscar Custance, Chemical identification of individual surface atoms by atomic force microscopy , *Nature* **446**, 64 (2007)
• Scanning Probe Microscopy investigation of self-organized perylenetetracarboxdiimide nanostructures at surfaces: structural and electronic properties".V. Palermo, A. Liscio, D. Gentilini, F. Nolde, K. Müllen, P. Samorì. *Small* **3**, 161-167 (2007);
• Kelvin Probe Force Microscopy study of surface charges photogeneration in all-thiophene photovoltaic blends. V. Palermo, G. Ridolfi, A.M. Talarico, L. Favaretto, G. Barbarella, N. Camaioni, P. Samorí, *Adv. Func. Mate.* **17**, 472 (2007).
• Quantitative measurement of the local surface potential of π-conjugated nanostructures: a Kelvin Probe Force Microscopy study. Andrea Liscio, Vincenzo Palermo, Desireè Gentilini, Fabian Nolde, Klaus Müllen, Paolo Samorì, *Advanced Functional Materials* **16,** 1407 – 1416 (2006)
• Scanning Force Microscopy on Molecular Nanostructures: Morphology, Properties and Nanofabrication (*in italian*).Cristiano Albonetti, Massimiliano Cavallini, Rajendra Kshirsagar, Fabio Biscarini "Microscopy in Italy"
• Electronic Characterization of Organic Thin Films by Kelvin Probe Force Microscopy. *V.* Palermo, M. Palma, P. Samori, *Advanced Materials* **18**, 145 (2006).
• Single atomic contact adhesion and dissipation in dynamic force microscopy*, N. Oyabu, P. Pou,* Y. Sugimoto, P. Jelinek, M. Abe, S. Morita and R. Perez, *Phys. Rev. Lett.* **92**, 106101 (2006)
•V. Palermo, S. Morelli , M. Palma, C. Simpson, F. Nolde, A. Herrmann, K. Müllen, P. Samorì, Nanoscale phase segregated supramolecular blends of a functionalized perylene-bis-dicarboximide and an all-benzenoid polycyclic aromatic hydrocarbon: architectures for organic solar cells. *ChemPhysChem.* **7**, 847 (2006)

Submitted

•C. Dietz, M. Zerson, C. Riesch, A.M. Gigler, R.W. Stark, N. Rehse and R. Magerle, Nanotomography with enhanced resolution using bimodal AFM, *Appl. Phys. Lett.* (submitted).
• Nicolas F. Martínez, Wojciech Kaminski, Carlos J. Gómez, Cristiano Albonetti, Fabio Biscarini , Ruben Perez and Ricardo Garcia, Molecular energy-dissipating processes in oligothiophene monolayers determined by phase-imaging force microscopy **,** *Advanced Materials*
• E.T. Herruzo, S. Patil and R. Garcia, Bimoal AFM imaging of antibodies in liquids, *Appl. Phys. Lett.* (submitted).

- M. Bauer, A.M. Gigler, C. Richter, R.W. Stark: "Visualizing stress in silicon microcantilevers using scanning confocal Raman spectroscopy", *Microelectron. Eng.*, in press
- Nikodem Tomczak and Julius Vancso, *Microcontact printed poly(amidoamine) dendrimer monolayers on silicon oxide surface*, submitted to *European Polymer Journal Macromolecular Nanotechnology.*
- Nikodem Tomczak and Julius Vancso, *Elasticity of single poly (amino amine) dendrimers*, *Physical Review Letters*.